

Structural and electrochemical stabilization enabling high-energy P3-type Cr-based layered oxide cathode for K-ion batteries

Wonseok Ko^{1,2} | Seokjin Lee^{1,2} | Hyunyoung Park^{1,2} | Jungmin Kang^{1,2} |
 Jinho Ahn^{1,2} | Yongseok Lee^{1,2} | Gwangeon Oh³ | Jung-Keun Yoo⁴ |
 Jang-Yeon Hwang^{3,5}  | Jongsoo Kim^{1,2} 

¹Department of Energy Science, Sungkyunkwan University, Suwon, Republic of Korea

²SKKU Institute of Energy Science and Technology (SIEST), Sungkyunkwan University, Suwon, Republic of Korea

³Department of Energy Engineering, Hanyang University, Seoul, Republic of Korea

⁴Carbon Composites Department, Korea Institute of Materials Science (KIMS), Changwon, Republic of Korea

⁵Department of Battery Engineering, Hanyang University, Seoul, Republic of Korea

Correspondence

Jongsoo Kim, Department of Energy Science, Sungkyunkwan University, Suwon 16419, Republic of Korea.
 Email: jongoonkim@skku.edu

Jang-Yeon Hwang, Department of Energy Engineering, Hanyang University, Seoul 04763, Republic of Korea.
 Email: jangyeonhw@hanyang.ac.kr

Funding information

Korea Institute of Materials Science, Grant/Award Number: PNK9370; National Research Foundation of Korea, Grant/Award Numbers: NRF-2021R1A2C1014280, NRF-2022R1C1C1011058, NRF-2022M3H446401037201; Korea Institute of Science and Technology, Grant/Award Number: 2E32581-23-092

Abstract

Layered-type transition metal (TM) oxides are considered as one of the most promising cathodes for K-ion batteries because of the large theoretical gravimetric capacity by low molar mass. However, they suffer from severe structural change by de/intercalation and diffusion of K⁺ ions with large ionic size, which results in not only much lower reversible capacity than the theoretical capacity but also poor power capability. Thus, it is important to enhance the structural stability of the layered-type TM oxides for outstanding electrochemical behaviors under the K-ion battery system. Herein, it is investigated that the substitution of the appropriate Ti⁴⁺ contents enables a highly enlarged reversible capacity of P3-type K_xCrO₂ using combined studies of first-principles calculation and various experiments. Whereas the pristine P3-type K_xCrO₂ just exhibits the reversible capacity of ~120 mAh g⁻¹ in the voltage range of 1.5–4.0 V (vs. K⁺/K), the ~0.61 mol K⁺ corresponding to ~150 mAh g⁻¹ can be reversible de/intercalated at the structure of P3-type K_{0.71}[Cr_{0.75}Ti_{0.25}]O₂ under the same conditions. Furthermore, even at the high current density of 788 mA g⁻¹, the specific capacity of P3-type K_{0.71}[Cr_{0.75}Ti_{0.25}]O₂ is ~120 mAh g⁻¹, which is ~81 times larger than that of the pristine P3-type K_xCrO₂. It is believed that this research can provide an effective strategy to improve the electrochemical performances of the cathode materials suffered by severe structural change that occurred during charge/discharge under not only K-ion battery system but also other rechargeable battery systems.

This is an open access article under the terms of the [Creative Commons Attribution](https://creativecommons.org/licenses/by/4.0/) License, which permits use, distribution and reproduction in any medium, provided the original work is properly cited.

© 2023 The Authors. *Carbon Energy* published by Wenzhou University and John Wiley & Sons Australia, Ltd.

KEYWORDS

cathodes, first-principles calculations, layered-type oxide materials, potassium-ion batteries, structural stabilization

1 | INTRODUCTION

Since the usage of fossil fuels has caused many environmental problems such as global warming, fine dust, air pollution, and so forth,^{1,2} it is required to develop environment-friendly energy sources and efficient energy storage systems (ESSs).^{2,3} Lithium-ion batteries (LIBs) gain great attention as one of the most representative ESSs, owing to their high energy densities.^{4,5} Thus, their application is being enlarged from small electronic devices to electric vehicles, and the demands for LIBs are explosively increasing in the world. Because of limited and concentrated Li sources on the Earth, however, many people worry that a reliable supply of Li sources to satisfy the increased demands of LIBs would be gradually difficult in the near future, which would result in a huge increase in LIB production cost.^{6–8} Thus, it is required to develop a low-cost and reliable ESS as an alternative to LIBs for large-scale applications.^{9,10}

Among various candidates, potassium-ion batteries (KIBs) have been considered as the promising alternative to LIBs, owing to their cost merit by the usage of earth-abundant K resource and similar reaction mechanisms based on alkali-ions with LIBs. Moreover, it was known that the redox potential of K^+/K (-2.93 V vs. standard hydrogen electrode [SHE]) is similar to that of Li^+/Li (-3.04 V vs. SHE), which implies that KIBs can have the merits of not only low production cost but also high energy density.^{10–13} Thus, many research have focused on the development of novel and outstanding electrode materials for KIBs, and various cathode materials for KIBs have been reported, such as polyanion compounds, Prussian blue analogs, and layered-type oxides.^{14–23} In particular, layered-type transition metal (TM) oxide materials “ $K_x[TM]O_2$ ” have great attention because of their large gravimetric capacities.^{22,24} However, de/intercalation of K^+ ions with large ionic radius (~ 1.38 Å) results in structural instability of the layered structure, which leads to limitation of reversibly available capacities of $K_x[TM]O_2$.^{23,25} In terms of P3-type K_xCrO_2 (P3-KCO), its reversible capacity was just ~ 100 mAh g^{-1} in the voltage range of 1.5–3.8 V (vs. K^+/K), which is much smaller than the theoretical capacity (~ 217 mAh g^{-1}).²³

Thus, we found that the key to increase the reversible capacity of P3-KCO under the KIB system is the enhancement of the structural stability. In general, it was known that partial substitution of metal ions in $K_x[TM]O_2$ can effectively enhance structural stability such as suppression

of irreversible multiple-phase transitions. As reported in the previous studies, the redox reaction of Ti^{3+}/Ti^{4+} does not occur above 1.5 V (vs. K^+/K).^{26,27} It implies that the existence of Ti^{4+} in P3-KCO does not participate in the electrochemical reaction during K^+ de/intercalation and can play a role as the structural stabilizer to suppress the local structural change affected by the redox reaction of Cr^{3+}/Cr^{4+} . Because of larger valence state of Ti^{4+} than that of Cr^{3+} , however, too much substitution of Ti^{4+} (≥ 0.4 mol) in the P3-KCO structure should accompany decrease of total K^+ contents for charge neutrality, and it also resulted in a high decrease in the reversible capacity to less than ~ 50 mAh g^{-1} .²⁸ Thus, to stabilize the P3-KCO structure and enhance the electrochemical performances successfully, we thought that it is important to determine appropriate amounts of Ti-substitution in P3-KCO and to investigate the reaction mechanism and the structural change during K^+ de/intercalation in detail.^{27,29}

In this work, we demonstrated that P3-type $K_{0.71}[Cr_{0.75}Ti_{0.25}]O_2$ (P3-KCTO) can exhibit highly increased reversible capacity compared to P3-KCO through combined studies using first-principle calculations and various electrochemical and structural experiments. With stable retention of the P3-type layered structure even after de/intercalation of 0.71 mol K^+ , P3-KCTO delivered the specific capacity of ~ 150 mAh g^{-1} at the current density of 16 mA g^{-1} , and the electrochemical behaviors were stabilized with no multiple step in the charge/discharge profile. Moreover, even at 788 mA g^{-1} , the capacity was maintained up to ~ 120 mAh g^{-1} , corresponding to $\sim 81\%$ of the capacity measured at 16 mA g^{-1} . The cycle performance of P3-KCTO was also outstanding, with a capacity retention of $\sim 73\%$ for 300 cycles at ~ 158 mA g^{-1} . These electrochemical performances imply the excellence of P3-KCTO as the promising cathode for KIBs.

2 | EXPERIMENTAL SECTION

2.1 | Preparation of $NaCrO_2$ and $Na_{0.75}[Cr_{0.75}Ti_{0.25}]O_2$

Before the preparation of K_xCrO_2 and KCTO using Na^+/K^+ ion-exchange process, $NaCrO_2$ and $Na_{0.75}[Cr_{0.75}Ti_{0.25}]O_2$ were synthesized via solid-state method using Na_2CO_3 (purity: 99.5%), Cr_2O_3 (purity: 98.5%), and TiO_4 (purity: 99.9%) as precursors. The precursors were mixed with the

desired ratio using a planetary ball mill while 10 wt% excess of Na_2CO_3 to compensate for the losses during the calcinating process. The ball milling proceeded for 24 cycles with a 20 min milling at 500 rpm followed by a 10 min rest. After mixing, each mixed powder was pressed into a pellet and calcinated at 900°C for 10 h using an Ar gas flow (0.8 L min^{-1}) tube furnace. After synthesis, O3-type NaCrO_2 and $\text{Na}_{0.75}[\text{Cr}_{0.75}\text{Ti}_{0.25}]\text{O}_2$ were carbonized using pyromellitic acid (PA) ($\text{C}_{10}\text{H}_6\text{O}_2$; PA, purity: 96%) to improve the electronic conductivity. Each bare powder was mixed with PA at 85:15 weight ratio and pressed to make each pellet. These pellets were transferred to the Ar gas flow tube furnace and heated for 30 min at 550°C .

2.2 | Na^+/K^+ ion-exchange process for $\text{K}_x[\text{Cr}_{0.75+y}\text{Ti}_{0.25-y}]\text{O}_2$

We prepared P3- $\text{K}_x[\text{Cr}_{0.75+y}\text{Ti}_{0.25-y}]\text{O}_2$ via Na^+/K^+ ion-exchange process using electrochemical reaction under K-system because they are hard to synthesize directly via the solid-state method. Using prepared electrodes of $\text{Na}_{0.75+y}[\text{Cr}_{0.75+y}\text{Ti}_{0.25-y}]\text{O}_2$, K-cells were assembled and the charge/discharge was carried out in the voltage range of 1.5–3.8 V (NaCrO_2) or 1.5–4.0 V (others) for 100 cycles. After cycling, these coin cells were disassembled in an Ar-filled glove box, and resultant electrodes were washed with dimethyl carbonate over five times and then dried.

2.3 | Materials characterization

The crystal structure and information were analyzed using X-ray diffraction (XRD) (PANalytical Empyrean) with $\text{Mo K}\alpha$ radiation ($\lambda = 0.70930 \text{ \AA}$), and structural data were collected over the 2θ range of 4.6° – 34.3° with a step size of under 0.01° . For XRD analyses, powder samples were directly used, but electrode samples were sealed with Kapton tape to prevent air and moisture contact. The collected XRD patterns were converted to fit the $\text{Cu K}\alpha$ radiation ($\lambda = 1.54178 \text{ \AA}$). Rietveld refinement was performed using FullProf software. The microstructure of each sample was examined using field-emission scanning electron microscopy (FE-SEM; JEOL JSM-7600F; at the Sungkyunkwan University) at an accelerating voltage of 15 kV and high-resolution transmission electron microscopy (TEM; JEOL JEM-F200; at the National Center for Inter-university Research Facilities [NCIRF] at Seoul National University) at accelerating voltages of 80–120 kV. The Cr K-edge and Ti K-edge X-ray absorption spectroscopy spectra were obtained at beamline 7D at the PAL using Cr metal foils and Ti metal foils as references.

2.4 | Electrochemical characterization

To prepare the electrode, carbonized active material, carbon nanotube, and polyvinylidene fluoride were mixed in an 82.35:7.65:10 weight ratio with *N*-methyl-2-pyrrolidone, and the mixed slurry was applied onto Al foil with $200 \mu\text{m}$ thickness and dried in a vacuum oven at 100°C . After drying, the mass loading of the active material on the Al foil was $\sim 3 \times 10^{-3} \text{ g cm}^{-2}$.

All electrochemical reactions were performed using an automatic battery charge/discharge test system (WBCS 3000; WonATech) under the same K-system. R2032-type coin cell parts were used, and all coin cells were assembled in an Ar-filled glove box. To assemble the coin cell, electrodes were punched into 10π -mm diameter disks, and Whatman GF/F glass fiber filter, 0.5 M of KPF_6 in a 1:1 vol/vol mixture of ethylene carbonate, and diethyl carbonate and K-metal were used as the separator, electrolyte, and counter electrode, respectively.

2.5 | Computational details

In this work, all calculations of density functional theory (DFA) were processed using the Vienna ab initio Simulation Package and projector-augmented wave. Moreover, we used the Perdew–Burke–Ernzerhof parametrization of the generalized gradient approximation (GGA) for the exchange–correlation functional. The supercell structure of K_xCrO_2 and $\text{K}_x[\text{Cr}_{0.75}\text{Ti}_{0.25}]\text{O}_2$ was $2 \times 2 \times 1$, and k-point grid was $20 \times 20 \times 4$. The GGA + *U* method was adopted to address the localization of the d-orbital in Cr ions and Ti ions, with a *U* eff value of 3.7 and 1.5 eV, as used in previous studies.^{29,30} A kinetic energy cutoff of 500 eV was used in all the calculations, and all the structures were optimized until the force in the unit cell converged to within 0.03 eV \AA^{-1} . Cluster-assisted statistical mechanics (CASM) software was used to generate all the K^+ /vacancy configurations for each composition, followed by full DFT calculations on a maximum of 20 configurations with the lowest electrostatic energy for each composition used to obtain the convex hull plot of $\text{K}_x[\text{Cr}_{0.75}\text{Ti}_{0.25}]\text{O}_2$. Nudged elastic band (NEB) calculations were performed to determine the activation barrier for K^+ diffusion in the $\text{K}_x[\text{Cr}_{0.75}\text{Ti}_{0.25}]\text{O}_2$ structure. To perform the calculations, five intermediate images were generated between each K site. These structures were then calculated using the NEB algorithm with fixed lattice parameters and free internal atomic positions. The table of contents figure, crystal structure with NEB calculation results for K^+ diffusion pathways, and crystal structures based on the results of

the cluster-expansion method were drawn using VESTA software.

3 | RESULTS AND DISCUSSION

P3-KCTO was prepared through the ion-exchange process from O3-Na_{0.75}[Cr_{0.75}Ti_{0.25}]O₂ (O3-NCTO), since it is difficult to directly synthesize P3-KCTO as a pure P3-type layered structure by conventional solid-state methods (Figure S1). The electrode was fabricated using O3-NCTO for ion exchange, and TEM analysis revealed that there was no significant change in the morphology of O3-NCTO particles before and after electrode fabrication (Figure S2). Moreover, as a result of energy-dispersive X-ray spectroscopy (EDS)-based elemental mapping of TEM (Figure S3), it was confirmed that Na, Cr, and Ti elements were homogeneously distributed in the O3-NCTO particle with the following atomic ratio: Na:Cr:Ti = ~0.75:~0.75:~0.25. The detailed synthesis process of ion exchange is arranged in Section 2. Through Rietveld refinement based on the XRD pattern (Figure 1A), it was verified that P3-KCTO was successfully prepared without any impurities or second phases. Its crystal structure was composed of pure rhombohedral structure with *R3m* space group, and the lattice parameters of *a* and *c* were ~2.93357(13) and ~19.0408(14) Å, respectively, which is clearly distinct from the crystal structure of O3-NCTO (Figure S4). The low reliable factors ($R_p = 4.82\%$, $R_1 = 6.20\%$, $R_F = 3.21\%$, $\chi^2 = 0.466\%$) indicate high accuracy of the Rietveld refinement. The detailed structural information, such as atomic position, isotropic parameter, and occupancy of P3-KCTO and O3-NCTO, was tabulated and is presented in Tables S1 and S2. Based on the structural information from the Rietveld refinement results, we also confirmed that the stacking order of A-B-C-A-B-C in O3-NCTO (Figure S5) had clearly changed to P3, likely A-B-B-C-C-A (Figure 1B), through an electrochemical ion-exchange process. Moreover, it was verified that ~0.71 mol K⁺ exists in the P3-KCTO structure, which implies successful preparation of P3-KCTO. Using TEM and EDS-based elemental mapping, we also investigated the morphology and atomic ratio of P3-KCTO. As shown in Figure 1C, the average particle size of P3-KCTO was ~600 nm, and K, Cr, and Ti elements were homogeneously distributed in the particle with the following atomic ratio: K:Cr:Ti = ~0.71:~0.75:~0.25. The particle size and morphology were confirmed through SEM analysis (Figure S6). Moreover, the inductively coupled plasma (ICP) results (Table S3) indicate that the atomic ratio of K:Cr:Ti in P3-KCTO was ~0.71:~0.75:~0.25, and any Na elements were not detected, which is well matched with the TEM-based EDS results. In addition, it was verified through synchrotron-based X-ray absorption near-edge structure

(XANES) analyses that the oxidation states of Cr and Ti in P3-KCTO are +3 and +4, respectively (Figure 1D,E).

To verify the enhanced electrochemical performances by substitution of 0.25 mol Ti⁴⁺ ions in P3-KCO, we compared the charge/discharge curves of P3-KCTO and P3-KCO at ~16 mA g⁻¹. Whereas the discharge capacity of P3-KCO was just ~118.8 mAh g⁻¹, P3-KCTO delivered a discharge capacity of ~147.9 mAh g⁻¹ (Figure S7), which is much larger than the other P3-KCO with substitution of above 0.4 mol Ti.²⁸ Moreover, the charge/discharge profile of P3-KCTO was smooth and not complex, which is clearly different from that of P3-KCO with multiple steps.³¹ In addition, in the case of P3-KCTO, the cathodic and anodic peaks were demonstrated in the dQ/dV profile (Figure S8), which indicates that during cycling, intercalation-based reactions, but not surface reactions, occur. This result implies that the overall electrochemical behaviors of P3-KCTO were more stably occurring than those of P3-KCO, which is due to structural stabilization by Ti-substitution in the structure. This structural stabilization can also result in the highly enhanced power capability of P3-KCO. As shown in Figure 2A,B, P3-KCTO exhibited a large specific capacity of ~119.4 mAh g⁻¹ even at the current density of 788 mA g⁻¹, which corresponds to ~81% of the capacity measured at 16 mA g⁻¹. Moreover, the outstanding power capability of P3-KCTO was confirmed through further electrochemical tests using the high active material loading mass (= ~6 × 10⁻³ cm g⁻¹) (Figure S9). In terms of P3-KCO, on the other hand, its capacity retention at 788 mA g⁻¹ was just ~56.3 mAh g⁻¹, which is less than ~55.0% of the capacity at 16 mA g⁻¹ (Figure S10). Furthermore, P3-KCTO showed an excellent cycle life with a capacity retention of above ~73% after 300 cycles at 158 mA g⁻¹ (Figure 2C). To understand the effects of 0.25 mol Ti⁴⁺-substitution in P3-KCO in detail, we performed first-principles calculation on P3-KCTO. Using CASM software,³² we prepared the K⁺/vacancies configurations of O3- and P3-K_x[Cr_{0.75}Ti_{0.25}]O₂ compositions (0 ≤ *x* ≤ 1), and to increase the reliability of the calculation, we considered 20 configurations for each composition. Based on the prepared configurations, we conducted first-principles calculation using the cluster-expansion method to obtain the formation energy for each configuration. By comparing the formation energy of O3- and P3-K_x[Cr_{0.75}Ti_{0.25}]O₂ (*x* = 0 and 1), it was confirmed that P3-K₀[Cr_{0.75}Ti_{0.25}]O₂ and O3-K₁[Cr_{0.75}Ti_{0.25}]O₂ are the most stable composition for each K⁺ composition. Taking P3-K₀[Cr_{0.75}Ti_{0.25}]O₂ and O3-K₁[Cr_{0.75}Ti_{0.25}]O₂ composition as references, the convex hull plot for K_x[Cr_{0.75}Ti_{0.25}]O₂ (0 ≤ *x* ≤ 1) (Figure 2D) was described based on their relative formation energies (Tables S4 and S5), allowing for easier visualization of not

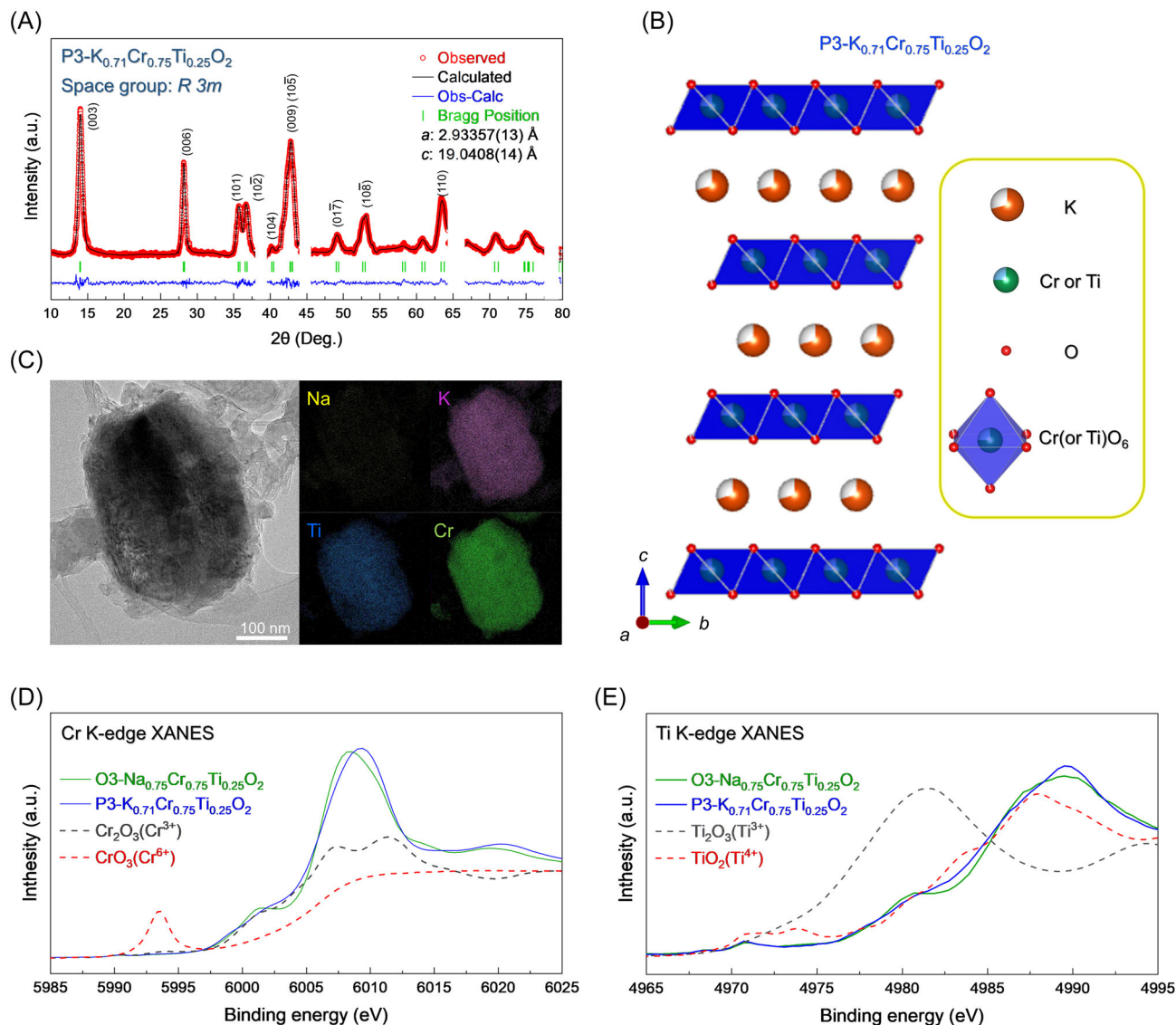


FIGURE 1 (A) Rietveld refinement of XRD pattern and (B) corresponding crystal structure of P3-K_{0.71}[Cr_{0.75}Ti_{0.25}]O₂. (C) TEM-EDS mapping of P3-K_{0.71}[Cr_{0.75}Ti_{0.25}]O₂ electrode. Ex situ analyses of P3-K_{0.71}[Cr_{0.75}Ti_{0.25}]O₂ on (D) Cr K-edge XANES spectra and (E) Ti K-edge XANES spectra.

only the existence of stable intermediate phases between the end compositions but also the energy difference between two phases related to redox potentials, compared to the original plot based on the real formation energies. The relative formation energies used to describe the convex hull plot were derived using the following equation:

$$E_{\text{formation}} = \frac{E(K_x[\text{Cr}_{0.75}\text{Ti}_{0.25}]\text{O}_2) + (1-x)E(\text{P3-K}_0[\text{Cr}_{0.75}\text{Ti}_{0.25}]\text{O}_2) + xE(\text{O3-K}_1[\text{Cr}_{0.75}\text{Ti}_{0.25}]\text{O}_2)}{2} \quad (1)$$

And then, we predicted the theoretical redox potentials of K_x[Cr_{0.75}Ti_{0.25}]O₂ as a function of K contents using the following equation:

$$V = \frac{E(K_{x_2}[\text{Cr}_{0.75}\text{Ti}_{0.25}]\text{O}_2) - E(K_{x_1}[\text{Cr}_{0.75}\text{Ti}_{0.25}]\text{O}_2) - (x_1 - x_2)E[K]}{(x_1 - x_2)F} \quad (2)$$

where *V* is the average redox potential between lowest formation energy each of K_{x₂}[Cr_{0.75}Ti_{0.25}]O₂ and K_{x₁}[Cr_{0.75}Ti_{0.25}]O₂, *E*[K] is formation energy of K

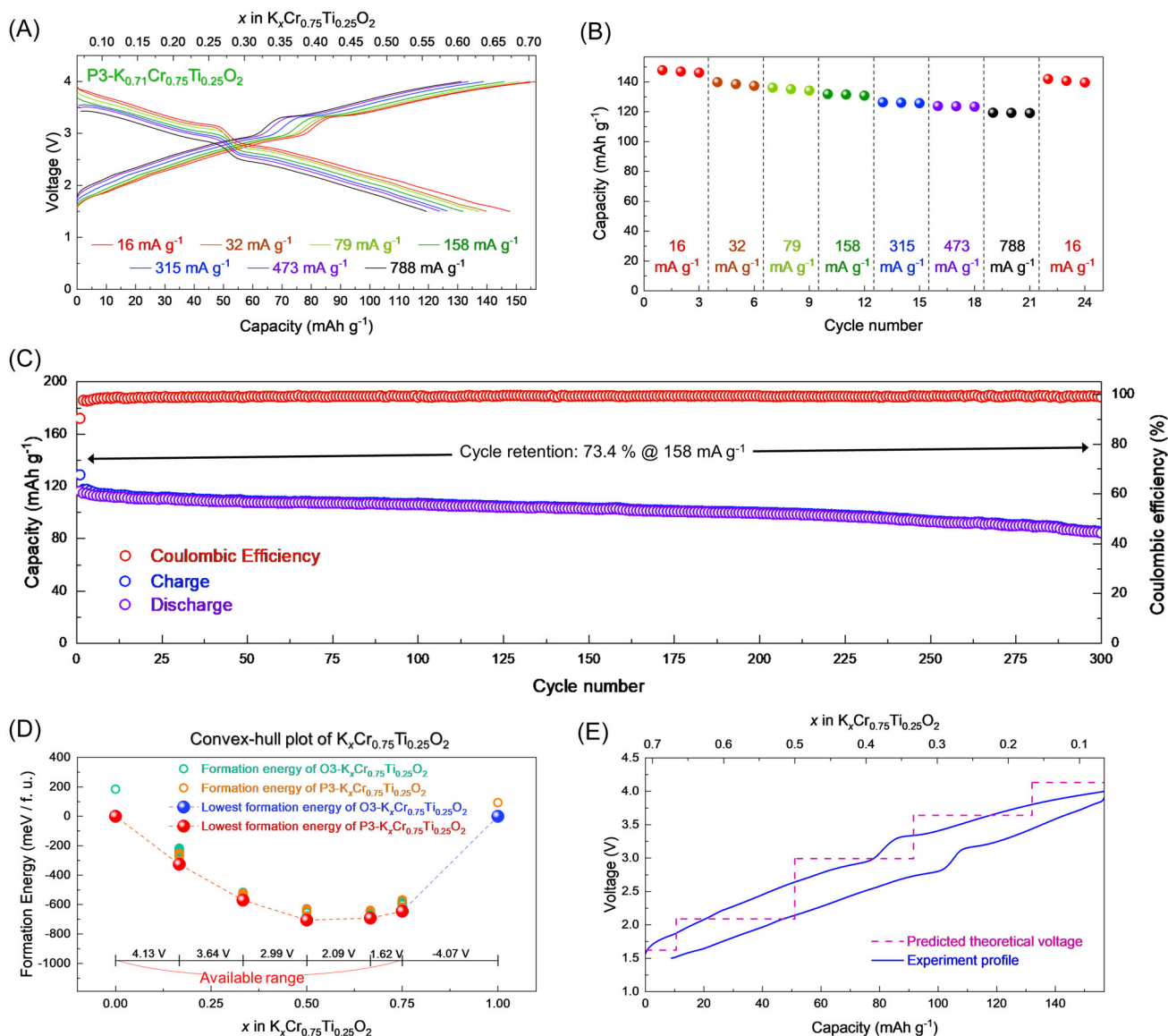


FIGURE 2 (A) Charge/discharge profiles and (B) power capability of $\text{P3-K}_x[\text{Cr}_{0.75}\text{Ti}_{0.25}]\text{O}_2$ at various current densities. (C) Capacities of charge/discharge and Coulombic efficiency of $\text{P3-K}_x[\text{Cr}_{0.75}\text{Ti}_{0.25}]\text{O}_2$ over 300 cycles at 158 mA g^{-1} . (D) Convex hull plot of O3- and $\text{P3-K}_x[\text{Cr}_{0.75}\text{Ti}_{0.25}]\text{O}_2$ configurations ($0 \leq x \leq 1$). (E) Comparison of the calculated redox potential of $\text{P3-K}_x[\text{Cr}_{0.75}\text{Ti}_{0.25}]\text{O}_2$ and its experimentally measured cycle curves at 16 mA g^{-1} .

metal, and F means the Faraday constant. These results indicate that ~ 0.7 mol K^+ can be reversibly de/intercalated at the structure of $\text{P3-K}_x[\text{Cr}_{0.75}\text{Ti}_{0.25}]\text{O}_2$ at the available voltage range. Figure 2E shows that the theoretical redox potentials of $\text{P3-K}_x[\text{Cr}_{0.75}\text{Ti}_{0.25}]\text{O}_2$ are well matched with the experimentally measured charge/discharge profile.

In addition, we compared the theoretical structural changes of $\text{P3-K}_x[\text{Cr}_{0.75}\text{Ti}_{0.25}]\text{O}_2$ and $\text{P3-K}_x\text{CrO}_2$ using first-principle calculation. As presented in Figure 3A,B, it was verified that the theoretically predicted difference of c -lattice parameter between $\text{P3-K}_{0.17}[\text{Cr}_{0.75}\text{Ti}_{0.25}]\text{O}_2$ and $\text{P3-K}_{0.86}[\text{Cr}_{0.75}\text{Ti}_{0.25}]\text{O}_2$ was just $\sim 0.42\%$ whereas that between

$\text{P3-K}_{0.17}\text{CrO}_2$ and $\text{P3-K}_{0.86}\text{CrO}_2$ was larger than $\sim 3.19\%$. Moreover, we confirmed that the difference of the average Cr-O bonding distance in the CrO_6 octahedra of $\text{P3-K}_x[\text{Cr}_{0.75}\text{Ti}_{0.25}]\text{O}_2$ was only $\sim 0.05977 \text{ \AA}$ (Figure 3C), which is smaller than that in the CrO_6 octahedra of $\text{P3-K}_x\text{CrO}_2$ ($\sim 0.08242 \text{ \AA}$) (Figure 3D). These results imply significantly suppressed structural change of P3-KCO by substitution of 0.25 mol Ti^{4+} ions, which is also consistent with outstanding electrochemical performances of P3-KCTO . Moreover, we calculated the theoretical activation barrier energy required for K^+ diffusion in the structure using first-principles calculation based on the NEB method. Figure 3E shows the predicted motion of K^+ diffusion in the structure, and it

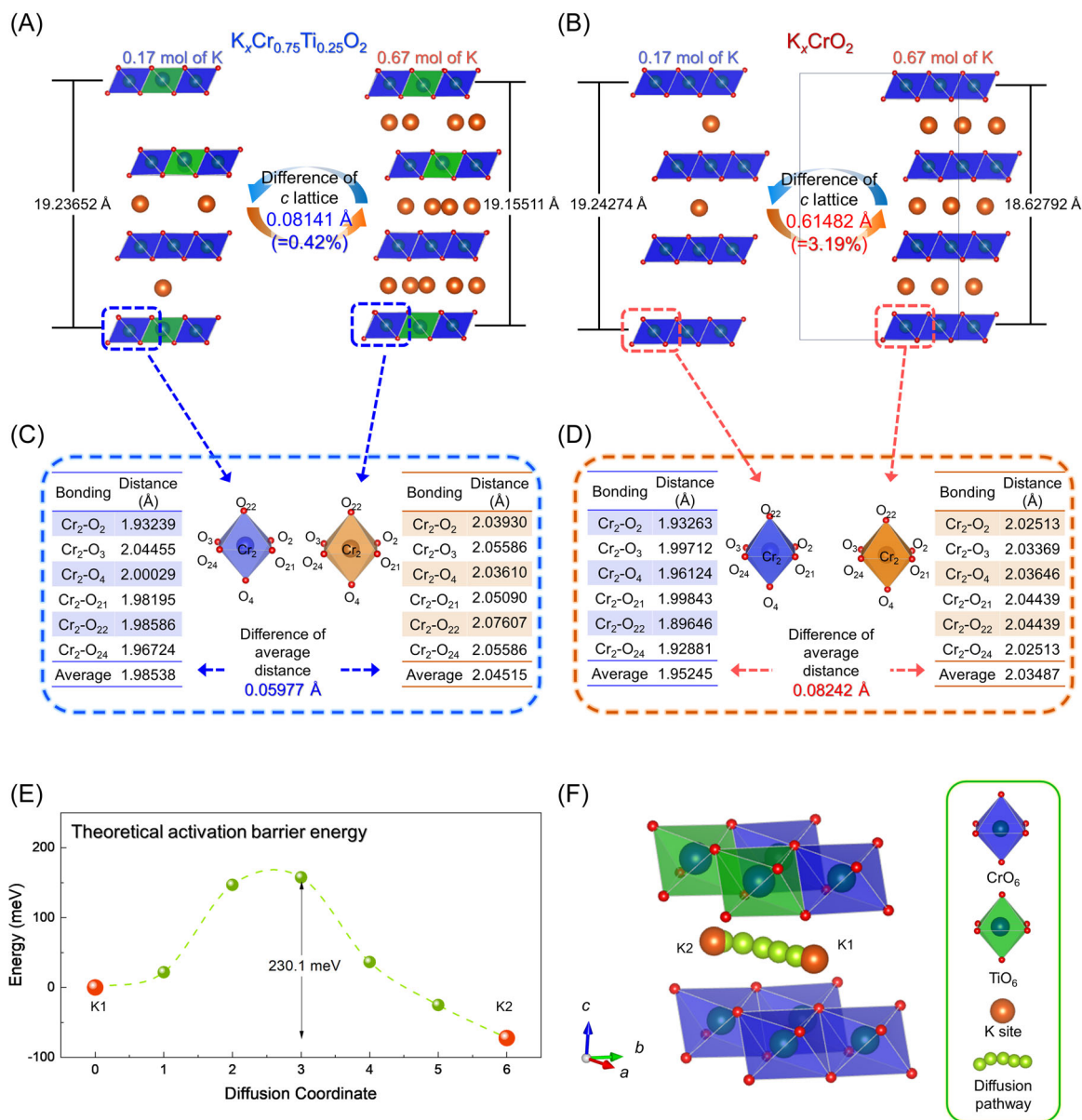


FIGURE 3 The difference in the c lattice ((A) $P3-K_x[Cr_{0.75}Ti_{0.25}]O_2$ and (B) $P3-K_xCrO_2$) and bonding length of CrO_6 octahedral between $x = 0.17$ and $x = 0.65$ ((C) $P3-K_x[Cr_{0.75}Ti_{0.25}]O_2$ and (D) $P3-K_xCrO_2$). (E) Predicted K^+ diffusion motion in $P3-K_x[Cr_{0.75}Ti_{0.25}]O_2$ and (F) predicted activation barrier energy for K^+ diffusion in the structure of $P3-K_x[Cr_{0.75}Ti_{0.25}]O_2$.

was verified that only ~230.1 meV was required for K^+ diffusion in the structure (Figure 3F). This value is similar to the theoretical activation barrier energy for Li^+ diffusion in $LiCoO_2$,³³ which is the reason for the great power capability of P3-KCTO. Moreover, as the bond dissociation energy of $Ti-O$ ($\Delta H_f^{298 K} = 661.9 \text{ kJ mol}^{-1}$) is higher than that of $Cr-O$ ($\Delta H_f^{298 K} = 427 \text{ kJ mol}^{-1}$), the substitution of Ti^{4+} ions facilitates strong bonding with neighboring oxygen atoms within the Cr-based layered structure.^{34,35} This strong bonding helps to stabilize the overall structure, preventing significant lattice distortions and structural degradation during K^+ de/intercalation processes. Furthermore, the nonparticipation of Ti^{4+} ions in the electrochemical reactions

during charge and discharge cycles is a significant advantage.³⁶ This characteristic allows Ti^{4+} to act as a stabilizer, preserving the structural integrity of the cathode material and increasing cyclability. In addition, we compared its electrochemical performances with those of other various cathode materials of KIBs reported up to date. As shown in Figure 4A,B and Table S6, it was clearly revealed that P3-KCTO exhibited larger energy density and better power capability than other cathode materials, which means that P3-KCTO has great merits as a promising cathode for KIBs.

The structural change and redox reaction of P3-KCTO during charge/discharge were also investigated through various experiments such as operando XRD, ex

situ extended X-ray absorption fine structure (EXAFS), and XANES. Figure 5A,B shows the operando XRD data measured during K^+ de/intercalation. It was verified that (003) and (006) peaks were slightly shifted to a lower 2θ angle during charging to 4.0 V (vs. K^+/K), and (101), (10 $\bar{2}$), and (105) peaks were shifted to a higher 2θ angle without significant phase transition. And then, the XRD peaks were returned to their original state during discharging to 1.5 V. Especially the intensities of the XRD peaks were also well recovered without severe structural degradation after charge/discharge. Moreover, Rietveld refinement based on the operando XRD patterns

indicated that the total change of c -lattice parameter of P3-KCTO during charge/discharge was only $\sim 3.09\%$ even though considerable amounts of K^+ ions with large ionic radius were de/intercalated at the structure (Figure 5C). Furthermore, through synchrotron-based ex situ EXAFS analysis, we confirmed that the local structural environments of P3-KCTO (Figure 6A,B), such as bond length of Cr–O, Cr–(Cr/Ti), Ti–O, and Ti–(Ti/Cr), were almost recovered even after charge/discharge, and total difference on the average length of Cr–O bond during charge/discharge was just $\sim 4.26\%$. Through the TEM-based analyses (Figure S11), it was verified that the particle size

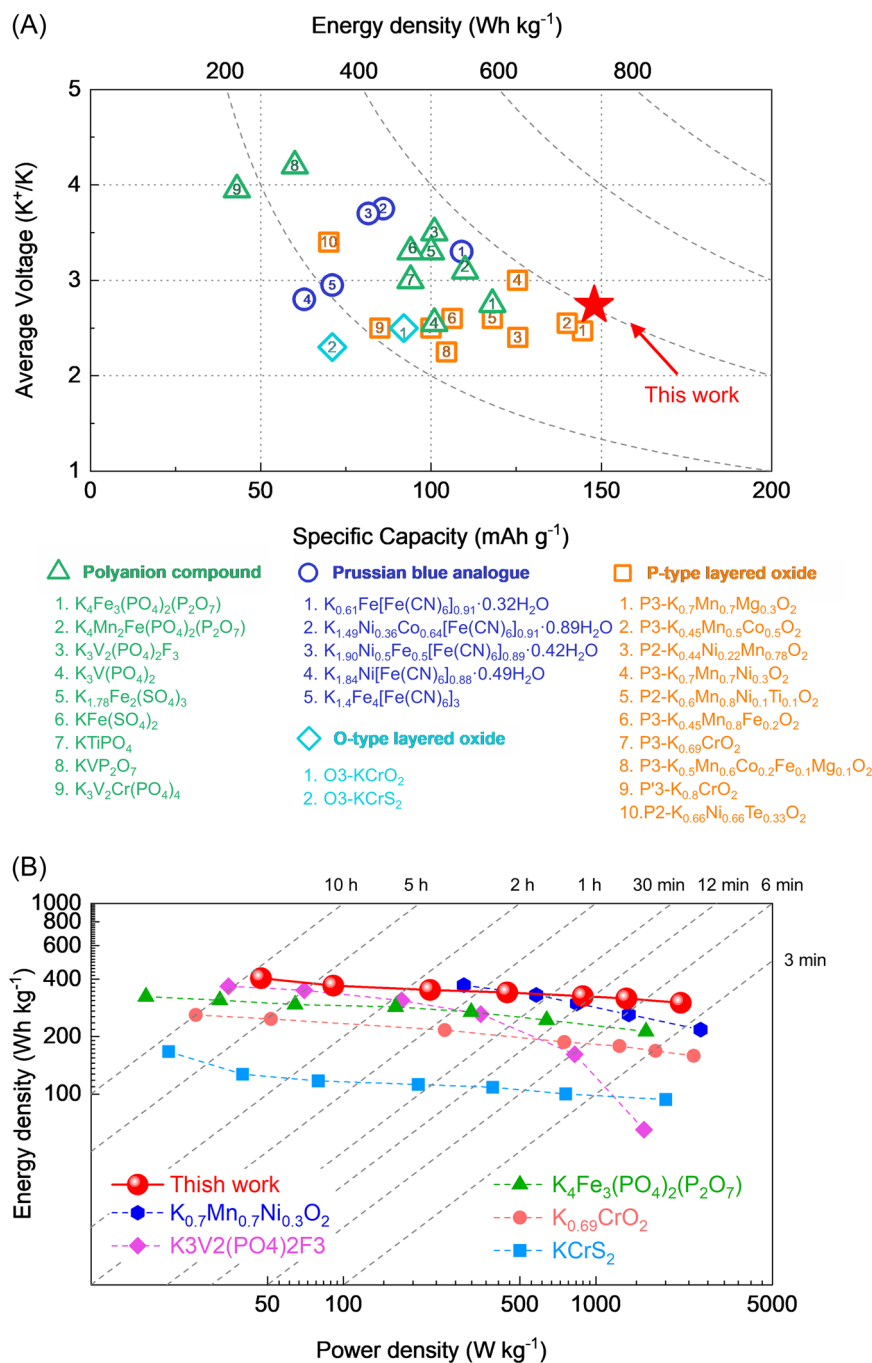
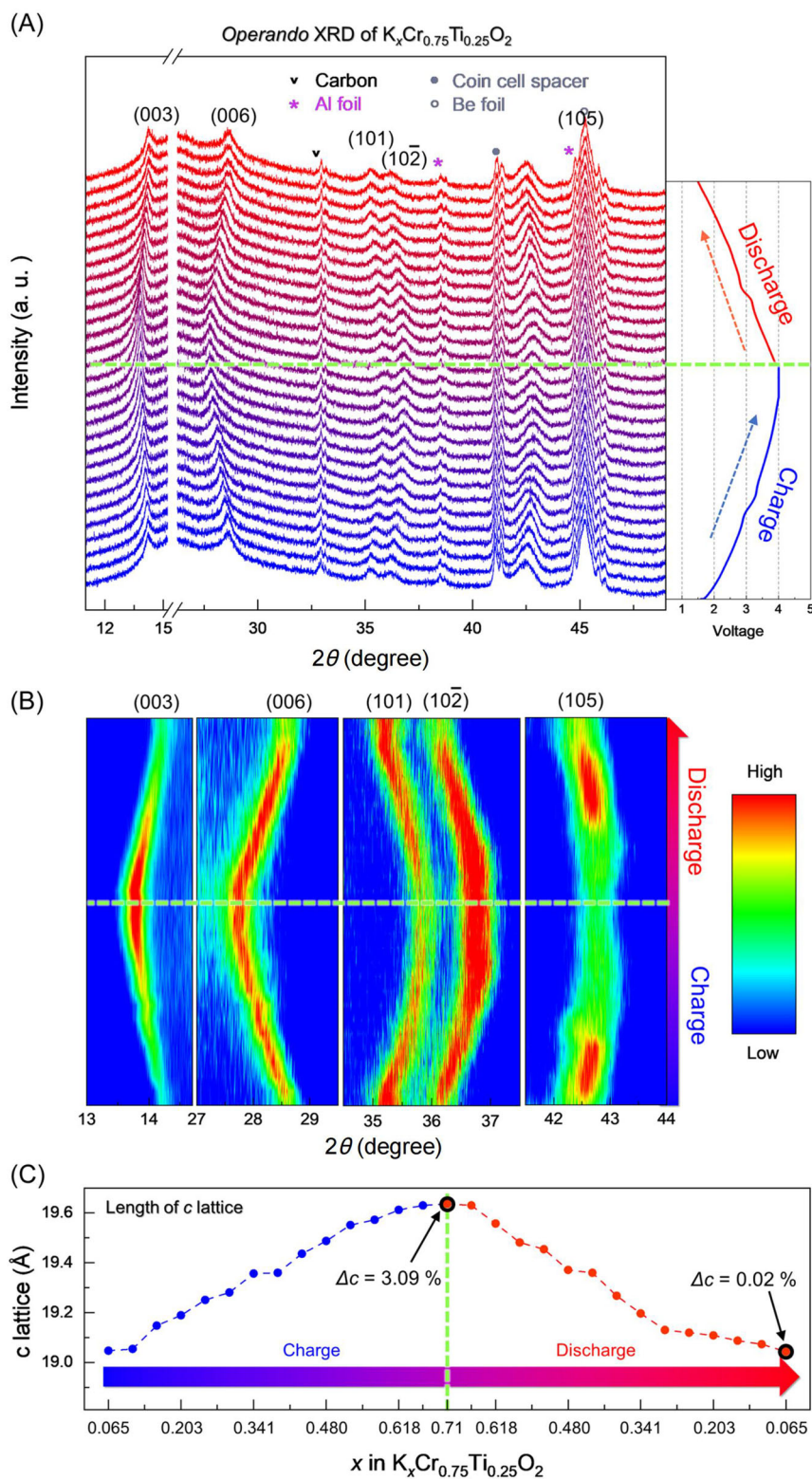


FIGURE 4 (A) Comparison of the electrochemical properties among $P3-K_x[Cr_{0.75}Ti_{0.25}]O_2$ and other cathode materials for K-ion batteries. (B) Ragone plot of $P3-K_x[Cr_{0.75}Ti_{0.25}]O_2$ and other cathode materials for KIBs (vs. K^+/K).^{6,15–17,21–23,37–58}

FIGURE 5 (A) Operando XRD pattern of $K_x[Cr_{0.75}Ti_{0.25}]O_2$ and (B) expansion of main peaks. (C) Changes in c lattice according to the amount to charge and discharge in the structure of $K_x[Cr_{0.75}Ti_{0.25}]O_2$.



of the as-prepared P3-KCTO with ~ 600 nm was similar to that of the cycled P3-KCTO, and their particle shapes were also similar to each other. Moreover, the well retention of morphologies of P3-KCTO without severe degradation or cracking after one cycle and 300 cycles was also confirmed through the SEM-based analyses

(Figure S12). These results indicate that high structural stability of P3-KCTO enables outstanding cycle performance under the KIB system. In addition, we investigated changes in oxidation states on Cr^{3+} and Ti^{4+} ions in the structure using the ex situ XANES analyses (Figure 6C,D). We verified that the Cr K-edge was

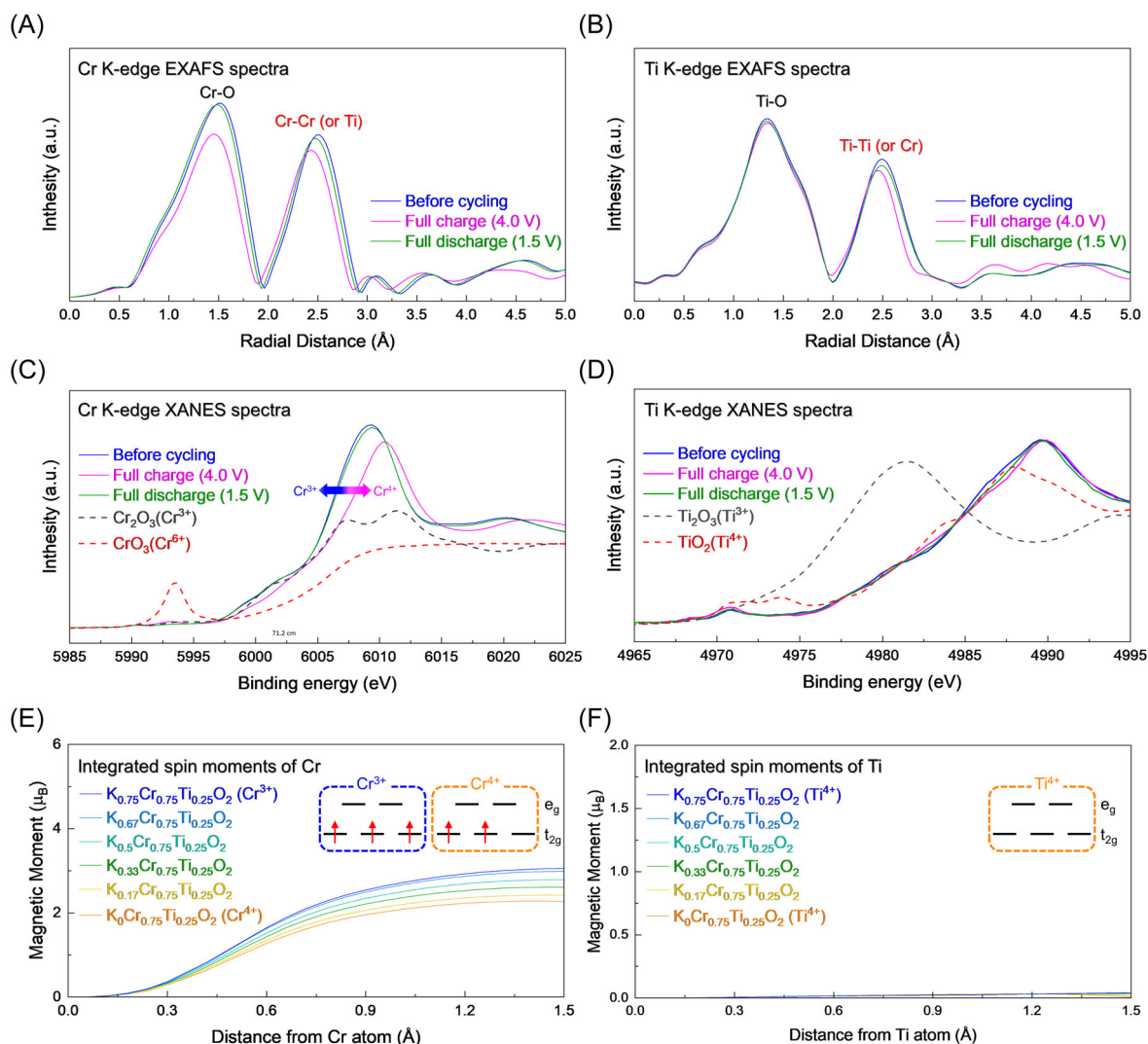


FIGURE 6 Ex situ (A) Cr K-edge and (B) Ti K-edge EXAFS spectra of $K_x[\text{Cr}_{0.75}\text{Ti}_{0.25}]\text{O}_2$. Ex situ (C) Cr K-edge and (D) Ti K-edge XANES spectra of $K_x[\text{Cr}_{0.75}\text{Ti}_{0.25}]\text{O}_2$. The integrated spin moments of $K_x[\text{Cr}_{0.75}\text{Ti}_{0.25}]\text{O}_2$: (E) Cr and (F) Ti.

shifted toward high energy level during charge, and then it was recovered to the original state, indicating $\text{Cr}^{3+/4+}$ redox reaction. On the other hand, the Ti K-edge was not changed even after charge/discharge and redox reaction of Ti^{4+} did not occur, which implies that existence of appropriate amounts of Ti^{4+} ions with a fixed valence state can successfully stabilize the P3-type Cr-based layered structure and prevent the large structural change that occurs during K^+ de/intercalation. Moreover, the redox reaction of P3-KCTO was also confirmed through comparison of the integrated spin moments predicted by first-principles calculation (Figure 6E,F). It was verified that the total spin moments of the Cr ion on P3- $K_x[\text{Cr}_{0.75}\text{Ti}_{0.25}]\text{O}_2$ decreased from 3 to 2, as the content of K increases, indicating that the valence state of the Cr ions in P3- $K_x[\text{Cr}_{0.75}\text{Ti}_{0.25}]\text{O}_2$ changed from +3 to +4. On the other hand, the total spin moment of Ti ions in

P3- $K_x[\text{Cr}_{0.75}\text{Ti}_{0.25}]\text{O}_2$ remained almost 0 and showed no significant variation with the increase in the amount of K, which suggests that there was no redox reaction on Ti ions during charge/discharge.

4 | CONCLUSION

In this study, we proposed P3-KCTO as a high-performance cathode material for KIBs. The P3-KCTO cathode was prepared from $\text{Na}_{0.75}[\text{Cr}_{0.75}\text{Ti}_{0.25}]\text{O}_2$ via electrochemical Na^+/K^+ ion-exchange method. Compared to the P3- $\text{K}_{0.69}\text{CrO}_2$ cathode, the P3-KCTO cathode delivered superior K^+ storage properties with reduced structural stress. A combination study of first-principles calculations and various experiments revealed that the substitution of 0.25 mol of Ti into Cr site lowers the

activation energy barrier for K^+ diffusion as well as improves the structural stability during charge/discharge process. Based on the $C_1^{3+/4+}$ redox reactions, the P3-KCTO cathode delivered a high discharge capacity of 147.9 mAh g^{-1} at 16 mA g^{-1} in the voltage of 1.5–4.0 V. At a high current density of 788 mA g^{-1} , the cathode delivered excellent cycling stability with capacity retention of 81% over 300 cycles and fast charge/discharge capability within 12 min. We believe that the proposed substitution strategy will provide new insights for improving the electrochemical properties of the layered structured cathode materials for KIBs.

ACKNOWLEDGMENTS

This work was supported by the National Research Foundation of Korea Grant, funded by the Korea Government Ministry of Education and Science Technology (NRF-2021R1A2C1014280, NRF-2022R1C1C1011058, NRF-2022M3H446401037201), Korea Institute of Materials Science (KIMS) of the Republic of Korea (PNK9370), and Korea Institute of Science and Technology (KIST) Institutional Program (No. 2E32581-23-092).

CONFLICT OF INTEREST STATEMENT

The authors declare that there are no conflicts of interest.

ORCID

Jang-Yeon Hwang  <https://orcid.org/0000-0003-3802-7439>

Jongsoon Kim  <https://orcid.org/0000-0002-7651-5516>

REFERENCES

- Vohra K, Vodonos A, Schwartz J, Marais EA, Sulprizio MP, Mickley LJ. Global mortality from outdoor fine particle pollution generated by fossil fuel combustion: Results from GEOS-Chem. *Environ Res*. 2021;195:110754.
- Davidsson Kurland S. Energy use for GWh-scale lithium-ion battery production. *Environ Res Commun*. 2020;2(1):012001.
- Zhang W, Maleki A, Birjandi AK, Alhuyi Nazari M, Mohammadi O. Discrete optimization algorithm for optimal design of a solar/wind/battery hybrid energy conversion scheme. *Int J Low Carbon Technol*. 2021;16(2):326-340.
- Tian Y, Zeng G, Rutt A, et al. Promises and challenges of next-generation “Beyond Li-ion” batteries for electric vehicles and grid decarbonization. *Chem Rev*. 2021;121(3):1623-1669.
- Kim H, Kim H, Ding Z, et al. Recent progress in electrode materials for sodium-ion batteries. *Adv Energy Mater*. 2016;6(19):1600943.
- Ko W, Park H, Jo JH, et al. Unveiling yavapaiite-type $KFe(SO_4)_2$ as a new Fe-based cathode with outstanding electrochemical performance for potassium-ion batteries. *Nano Energy*. 2019;66:104184.
- Ko W, Yoo J-K, Park H, et al. Exceptionally high-energy tunnel-type $V_{1.5}Cr_{0.5}O_{4.5}H$ nanocomposite as a novel cathode for Na-ion batteries. *Nano Energy*. 2020;77:105175.
- Kim SW, Seo DH, Ma X, Ceder G, Kang K. Electrode materials for rechargeable sodium-ion batteries: potential alternatives to current lithium-ion batteries. *Adv Energy Mater*. 2012;2(7):710-721.
- Hong W, Zhang Y, Yang L, et al. Carbon quantum dot micelles tailored hollow carbon anode for fast potassium and sodium storage. *Nano Energy*. 2019;65:104038.
- Liu Y, Tai Z, Zhang Q, et al. A new energy storage system: rechargeable potassium-selenium battery. *Nano Energy*. 2017;35:36-43.
- Yang Q, Wang Z, Xi W, He G. Tailoring nanoporous structures of Ge anodes for stable potassium-ion batteries. *Electrochem Commun*. 2019;101:68-72.
- Pramudita JC, Sehrawat D, Goonetilke D, Sharma N. An initial review of the status of electrode materials for potassium-ion batteries. *Adv Energy Mater*. 2017;7(24):1602911.
- Marcus Y. Thermodynamic functions of transfer of single ions from water to nonaqueous and mixed solvents: part 3—standard potentials of selected electrodes. *Pure Appl Chem*. 1985;57(8):1129-1132.
- Zhang Z, Wang R, Chen Z, et al. A micron-size carbon-free $K_3V_2O_2(PO_4)_2F$ cathode with high-rate performance for potassium-ion batteries. *Chem Eng J*. 2022;436:135235.
- Fedotov SS, Luchinin ND, Aksyonov DA, et al. Titanium-based potassium-ion battery positive electrode with extraordinarily high redox potential. *Nat Commun*. 2020;11:1484.
- Bodart J, Eshraghi N, Carabin T, et al. Spray-dried $K_3V(PO_4)_2/C$ composites as novel cathode materials for K-ion batteries with superior electrochemical performance. *J Power Sources*. 2020;480:229057.
- Huang B, Shao Y, Liu Y, Lu Z, Lu X, Liao S. Improving potassium-ion batteries by optimizing the composition of Prussian blue cathode. *ACS Appl Energy Mater*. 2019;2(9):6528-6535.
- Zhang J, Deng L, Feng M, Zeng L, Hu M, Zhu Y. Low-defect $K_2Mn[Fe(CN)_6]$ -reduced graphene oxide composite for high-performance potassium-ion batteries. *Chem Commun*. 2021;57(69):8632-8635.
- Ma X, Guo Y, Yu C, et al. Preparation of $K_2Fe[Fe(CN)_6]$ nanoparticles by improved electrostatic spray assisted precipitation technology as potassium-ion battery cathodes. *J Alloys Compd*. 2022;904:164049.
- Zhang Q, Didier C, Pang WK, et al. Structural insight into layer gliding and lattice distortion in layered manganese oxide electrodes for potassium-ion batteries. *Adv Energy Mater*. 2019;9(30):1900568.
- Deng T, Fan X, Chen J, et al. Layered P2-type $K_{0.65}Fe_{0.5}Mn_{0.5}O_2$ microspheres as superior cathode for high-energy potassium-ion batteries. *Adv Funct Mater*. 2018;28(28):1800219.
- Zhang X, Yang Y, Qu X, et al. Layered P2-type $K_{0.44}Ni_{0.22}Mn_{0.78}O_2$ as a high-performance cathode for potassium-ion batteries. *Adv Funct Mater*. 2019;29(49):1905679.
- Hwang J-Y, Kim J, Yu T-Y, Myung S-T, Sun Y-K. Development of P3- $K_{0.69}CrO_2$ as an ultra-high-performance cathode material for K-ion batteries. *Energy Environ Sci*. 2018;11(10):2821-2827.
- Li Y, Yang C, Zheng F, et al. Design of TiO_2/eC hierarchical tubular heterostructures for high performance potassium ion batteries. *Nano Energy*. 2019;59:582-590.

25. Komaba S, Hasegawa T, Dahbi M, Kubota K. Potassium intercalation into graphite to realize high-voltage/high-power potassium-ion batteries and potassium-ion capacitors. *Electrochem Commun.* 2015;60:172-175.
26. Liu J, Pang WK, Zhou T, et al. $\text{Li}_2\text{TiSiO}_5$: a low potential and large capacity Ti-based anode material for Li-ion batteries. *Energy Environ Sci.* 2017;10(6):1456-1464.
27. Liu Y, Liu J, Wu Y, et al. $\text{Na}_{1.68}\text{H}_{0.32}\text{Ti}_2\text{O}_3\text{SiO}_4 \cdot 1.76\text{H}_2\text{O}$ as a low-potential anode material for sodium-ion battery. *ACS Appl Energy Mater.* 2018;1(10):5151-5157.
28. Pandey AK, Campéon BDL, Konuma I, Yabuuchi N. P3-type layered $\text{K}_{0.6}\text{Cr}_{0.6}\text{Ti}_{0.4}\text{O}_2$ for potassium storage applications. *Energy Adv.* 2023;2(1):98-102.
29. Ko W, Cho M-K, Kang J, et al. Exceptionally increased reversible capacity of O_3 -type NaCrO_2 cathode by preventing irreversible phase transition. *Energy Storage Mater.* 2022;46:289-299.
30. Lee S, Kang J, Cho M, et al. High-energy P2-type Na-layered oxide cathode with sequentially occurred anionic redox and suppressed phase transition. *Appl Phys Rev.* 2022;9(4):041405.
31. Wang P-F, Yao H-R, Liu X-Y, et al. Ti-substituted $\text{Na-Ni}_{0.5}\text{Mn}_{0.5-x}\text{Ti}_x\text{O}_2$ cathodes with reversible O_3 - P_3 phase transition for high-performance sodium-ion batteries. *Adv Mater.* 2017;29(19):1700210.
32. Van der Ven A, Thomas JC, Xu Q, Bhattacharya J. Linking the electronic structure of solids to their thermodynamic and kinetic properties. *Math Comput Simul.* 2010;80(7):1393-1410.
33. Ning F, Li S, Xu B, Ouyang C. Strain tuned Li diffusion in LiCoO_2 material for Li ion batteries: a first principles study. *Solid State Ion.* 2014;263:46-48.
34. Lide DR. *CRC Handbook of Chemistry and Physics.* CRC Press.
35. Wu J, Hu G, Du K, et al. Inhibiting electrochemical phase transition of NaCrO_2 with long-cycle stability by surface fluorination treatment. *Electrochim Acta.* 2022;403:139641.
36. Zhao Q, Butt FK, Guo Z, et al. High-voltage P2-type manganese oxide cathode induced by titanium gradient modification for sodium ion batteries. *Chem Eng J.* 2021;403:126308.
37. Park H, Kim H, Ko W, et al. Development of $\text{K}_4\text{Fe}_3(\text{PO}_4)_2(\text{P}_2\text{O}_7)$ as a novel Fe-based cathode with high energy densities and excellent cyclability in rechargeable potassium batteries. *Energy Storage Mater.* 2020;28:47-54.
38. Kang J, Park H, Ko W, et al. Low-cost and high-power $\text{K}_4[\text{Mn}_2\text{Fe}](\text{PO}_4)_2(\text{P}_2\text{O}_7)$ as a novel cathode with outstanding cyclability for K-ion batteries. *J Mater Chem A.* 2021;9(15):9898-9908.
39. Lin X, Huang J, Tan H, Huang J, Zhang B. $\text{K}_3\text{V}_2(\text{PO}_4)_2\text{F}_3$ as a robust cathode for potassium-ion batteries. *Energy Storage Mater.* 2019;16:97-101.
40. Kang J, Ko W, Park H, et al. High-power rhombohedral $\text{Fe}_2(\text{SO}_4)_3$ with outstanding cycle-performance as Fe-based cathode for K-ion batteries. *Energy Storage Mater.* 2020;33:276-282.
41. Park WB, Han SC, Park C, et al. KVP_2O_7 as a robust high-energy cathode for potassium-ion batteries: pinpointed by a full screening of the inorganic registry under specific search conditions. *Adv Energy Mater.* 2018;8(13):201703099.
42. Wang J, Ouyang B, Kim H, Tian Y, Ceder G, Kim H. Computational and experimental search for potential poly-anionic K-ion cathode materials. *J Mater Chem A.* 2021;9(34):18564-18575.
43. Deng L, Qu J, Niu X, et al. Defect-free potassium manganese hexacyanoferrate cathode material for high-performance potassium-ion batteries. *Nat Commun.* 2021;12:2167.
44. Huang B, Liu Y, Lu Z. Prussian blue $[\text{K}_2\text{FeFe}(\text{CN})_6]$ doped with nickel as a superior cathode: an efficient strategy To enhance potassium storage performance. *ACS Sustainable Chem Eng.* 2019;7(19):16659-16667.
45. Zhu Y-H, Yang X, Bao D. High-energy-density flexible potassium-ion battery based on patterned electrodes. *Joule.* 2018;2(4):736-746.
46. Chong S, Yang J, Sun L, Guo S, Liu Y, Liu HK. Potassium nickel iron hexacyanoferrate as ultra-long-life cathode material for potassium-ion batteries with high energy density. *ACS Nano.* 2020;14(8):9807-9818.
47. Li L, Hu Z, Lu Y. A Low-strain potassium-rich prussian blue analogue cathode for high power potassium-ion batteries. *Angew Chem Int Ed.* 2021;60(23):13050-13056.
48. Qin M, Ren W, Meng J, et al. Realizing superior prussian blue positive electrode for potassium storage via ultrathin nanosheet assembly. *ACS Sustainable Chem Eng.* 2019;7(13):11564-11570.
49. Kim H, Seo D-H, Urban A, et al. Stoichiometric layered potassium transition metal oxide for rechargeable potassium batteries. *Chem Mater.* 2018;30(18):6532-6539.
50. Naveen N, Park WB, Singh SP. KCrS_2 Cathode with considerable cyclability and high rate performance: the first K^+ stoichiometric layered compound for potassium-ion batteries. *Small.* 2018;14:1803495.
51. Ramasamy HV, Senthilkumar B, Barpanda P, Lee Y-S. Superior potassium-ion hybrid capacitor based on novel P3-type layered $\text{K}_{0.45}\text{Mn}_{0.5}\text{Co}_{0.5}\text{O}_2$ as high capacity cathode. *Chem Eng J.* 2019;368:235-243.
52. Xiao Z, Meng J, Xia F, et al. K^+ modulated K^+ /vacancy disordered layered oxide for high-rate and high-capacity potassium-ion batteries. *Energy Environ Sci.* 2020;13(9):3129-3137.
53. Xu Y-S, Zhou Y-N, Zhang Q-H, et al. Layered oxides with solid-solution reaction for high voltage potassium-ion batteries cathode. *Chem Eng J.* 2021;412:128735.
54. Liu C, Luo S, Huang H, Liu X, Zhai Y, Wang Z. Fe-doped layered P3-type $\text{K}_{0.45}\text{Mn}_{1-x}\text{Fe}_x\text{O}_2$ ($x \leq 0.5$) as cathode materials for low-cost potassium-ion batteries. *Chem Eng J.* 2019;378:122167.
55. Xiao Z, Xia F, Xu L, et al. Suppressing the Jahn-Teller effect in Mn-based layered oxide cathode toward long-life potassium-ion batteries. *Adv Funct Mater.* 2021;32(14):2108244.
56. Naveen N, Han SC, Singh SP, Ahn D, Sohn K-S, Pyo M. Highly stable $\text{P}'3\text{-K}_{0.8}\text{CrO}_2$ cathode with limited dimensional changes for potassium ion batteries. *J Power Sources.* 2019;43:137-144.
57. Masese T, Yoshii K, Yamaguchi Y, et al. Rechargeable potassium-ion batteries with honeycomb-layered tellurates as high voltage cathodes and fast potassium-ion conductors. *Nat Commun.* 2018;9(1):3823.
58. Weng J, Duan J, Sun C, et al. Construction of hierarchical $\text{K}_{0.7}\text{Mn}_{0.7}\text{Mg}_{0.3}\text{O}_2$ microparticles as high capacity & long

cycle life cathode materials for low-cost potassium-ion batteries. *Chem Eng J.* 2020;392:123649.

SUPPORTING INFORMATION

Additional supporting information can be found online in the Supporting Information section at the end of this article.

How to cite this article: Ko W, Lee S, Park H, et al. Structural and electrochemical stabilization enabling high-energy P3-type Cr-based layered oxide cathode for K-ion batteries. *Carbon Energy.* 2024;6:e454. doi:10.1002/cey2.454